Understanding the regional pattern of projected future changes in extreme precipitation

S. Pfahl[1]*, P. A. O'Gorman[2] and E. M. Fischer[1]

Changes in extreme precipitation are among the most impact-relevant consequences of climate warming[1], yet regional projections remain uncertain due to natural variability[2] and model deficiencies in relevant physical processes[3,4]. To better understand changes in extreme precipitation, they may be decomposed into contributions from atmospheric thermodynamics and dynamics[5–7], but these are typically diagnosed with spatially aggregated data[8,9] or using a statistical approach that is not valid at all locations[10,11]. Here we decompose the forced response of daily regional scale extreme precipitation in climate-model simulations into thermodynamic and dynamic contributions using a robust physical diagnostic[8]. We show that thermodynamics alone would lead to a spatially homogeneous fractional increase, which is consistent across models and dominates the sign of the change in most regions. However, the dynamic contribution modifies regional responses, amplifying increases, for instance, in the Asian monsoon region, but weakening them across the Mediterranean, South Africa and Australia. Over subtropical oceans, the dynamic contribution is strong enough to cause robust regional decreases in extreme precipitation, which may partly result from a poleward circulation shift. The dynamic contribution is key to reducing uncertainties in future projections of regional extreme precipitation.

Climate models project a general intensification of extreme precipitation events during the twenty-first century on continental to global spatial scales[2,8,12,13], and this general large-scale amplification is consistent with observed trends in extreme precipitation[14–16]. To first order, the simulated enhancement of extreme precipitation can be attributed to the increasing atmospheric moisture content in a warming climate[5,6], which approximately follows the Clausius–Clapeyron equation. Other thermodynamic and dynamic factors also influence its magnitude—in particular, changes in the temperature lapse rate, in vertical wind velocities and in the temperature anomaly when the extreme events occur[8,9].

On regional scales, the change in extreme precipitation in a warming climate can differ substantially from the global-scale increase[12,17]. Such regional differences can be partly due to natural variability[2]. Nevertheless, the simulated forced response to global warming, the long-term response in the absence of internal variability, also exhibits regions with little change, and even substantial areas with decreases in extreme precipitation, in particular in the subtropics[12,17]. To understand the physical mechanisms causing these regional differences, previous studies have attempted to decompose the regional signal into thermodynamic and dynamic contributions using statistical methods[10,11], which rely on the empirical correlation of precipitation amount and vertical wind velocity at 500 hPa. Such statistical methods are not applicable for regions

in which the correlation of precipitation with the vertical velocity at 500 hPa is weak[10]. Some of the problematic regions for the statistical approach, such as the subtropics, are where the simulated change in extreme precipitation differs most prominently from the global-scale increase.

In this study, we apply a physical scaling diagnostic, which has so far been used for studying aggregated changes in precipitation extremes on large scales[8,9], to decompose the forced regional change in extreme precipitation in climate simulations from the Coupled Model Intercomparison Project Phase 5 (CMIP5) for the period 1950–2100 into thermodynamic and dynamic contributions. This scaling relates the precipitation amount during an extreme event, in our case the annual maximum daily precipitation P_e at each model grid point (often referred to as the Rx1day index), to the corresponding vertical pressure velocity ω_e and the vertical derivative of the saturation specific humidity q_s at constant saturation equivalent potential temperature θ^*:

$$P_e \sim -\left\{ \omega_e \left. \frac{\mathrm{d}q_s}{\mathrm{d}p} \right|_{\theta^*} \right\} \tag{1}$$

Here {.} indicates a mass-weighted vertical integral over the troposphere. This scaling relation can be derived assuming a moist-adiabatic, saturated ascent of air parcels[8] or, for the tropics, using an energy budget approach that does not require an assumption of large-scale saturated ascent[18]. The right-hand side of equation (1) is an estimate of the column integrated net condensation rate, and in general a precipitation efficiency must be included to convert the scaling to an equality; this efficiency factor is important for convective precipitation extremes on shorter timescales and smaller space scales than considered here[19]. In this study, we use daily mean temperature and vertical velocity profiles on pressure levels at the location and on the day of the annual maximum daily precipitation from 22 CMIP5 models to evaluate the right-hand side of equation (1) (see Methods).

Testing the suitability of the diagnostic estimate with CMIP5 models (Fig. 1) reveals that the scaling relationship (equation (1)) very accurately reproduces the actually simulated multi-model mean spatial pattern of annual maximum precipitation (Rx1day) in the present-day reference period 1981–2000 (spatial correlation of 0.99, root mean square difference of 5 mm d^{-1}). The scaling overestimates the simulated precipitation amount in some dry regions in the subtropics and underestimates it in moist regions in the tropics and over the ocean, as well as in regions of complex orography, such as along the west coast of North and South America (Supplementary Fig. 1), which may be related to either the approximations made in deriving the scaling or to not taking the


1
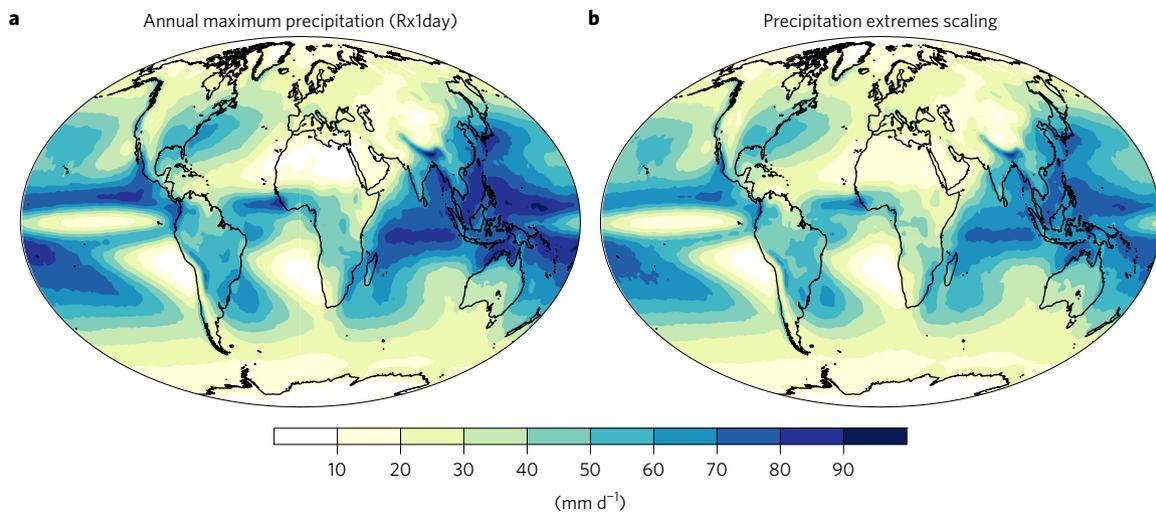
Figure 1 | Present-day precipitation extremes and scaling. a,b, Multi-model mean annual maximum precipitation Rx1day (in mm d^{-1}) (**a**) and precipitation extremes scaling (equation (1), in mm d^{-1}) (**b**), both averaged over the period 1981–2000.
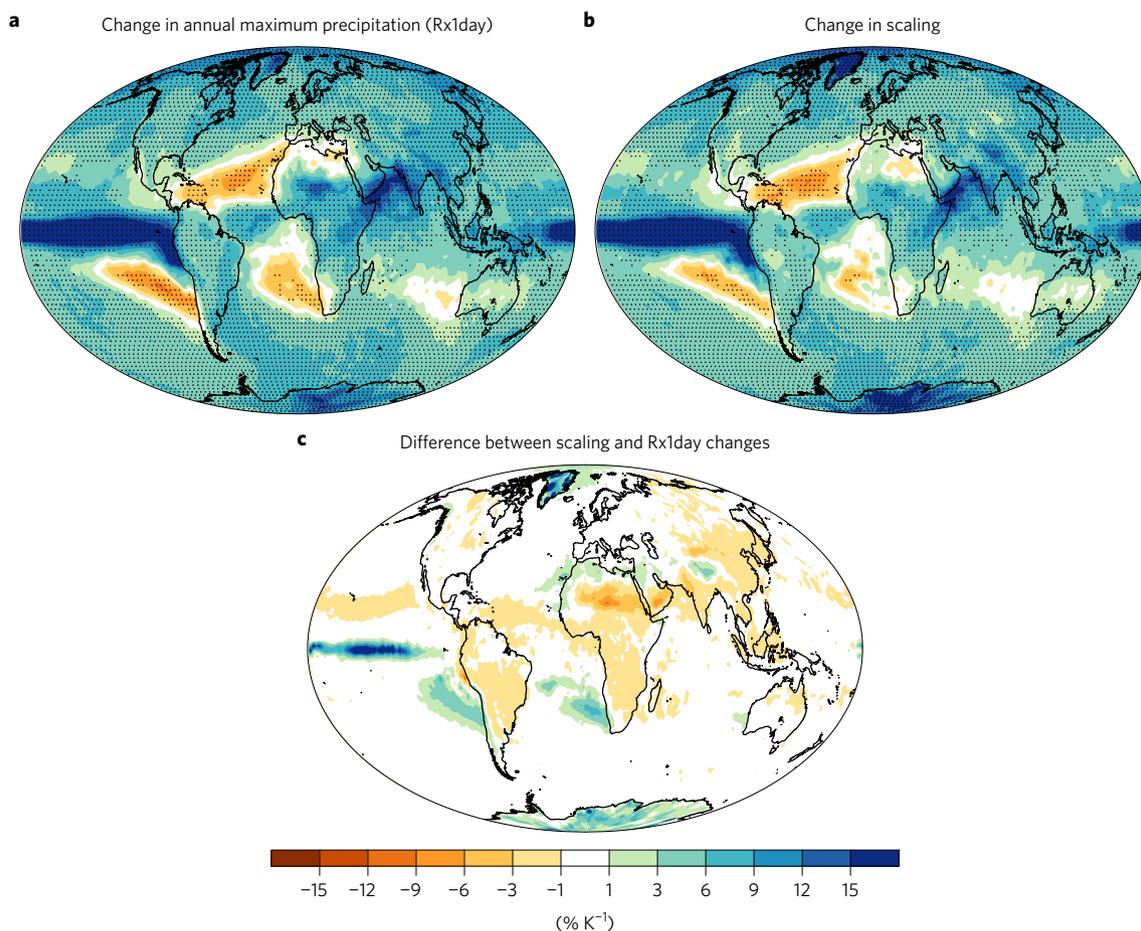
Figure 2 | Forced changes in precipitation extremes and scaling. a,b, Multi-model mean fractional changes in annual maximum precipitation Rx1day (**a**) and precipitation extremes scaling (**b**) per K global warming (in % K^{-1}) derived from a linear regression for the period 1950–2100. Stippling indicates that at least 80% of the models agree on the sign of change. A robust increase in Rx1day is found for 82% of the global land areas, and models do not agree on the sign of the change for the remaining 18%. **c,** Difference between fractional changes in the scaling and Rx1day.

precipitation efficiency factor into account. The agreement between spatial patterns of simulated Rx1day and scaling is also very good for individual models (spatial correlation > 0.94 in all models), and when considering seasonal instead of annual precipitation maxima (Supplementary Fig. 2).

To investigate simulated changes in heavy precipitation using the scaling diagnostic, we first quantify the multi-model mean forced change of Rx1day over the period 1950–2100 through a linear regression of Rx1day against global mean temperature (Fig. 2a). Consistent with previous studies[12,17], precipitation extremes are
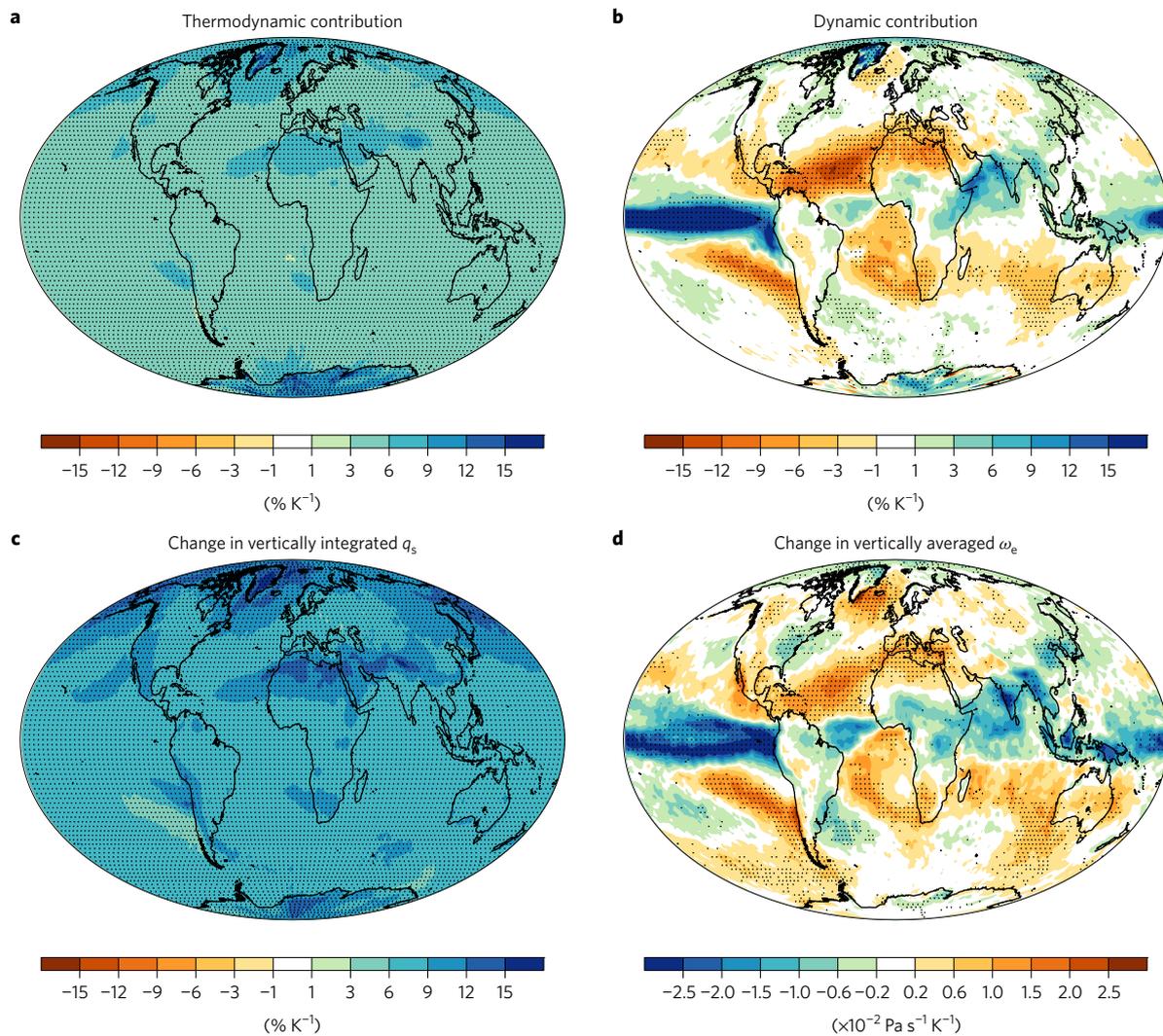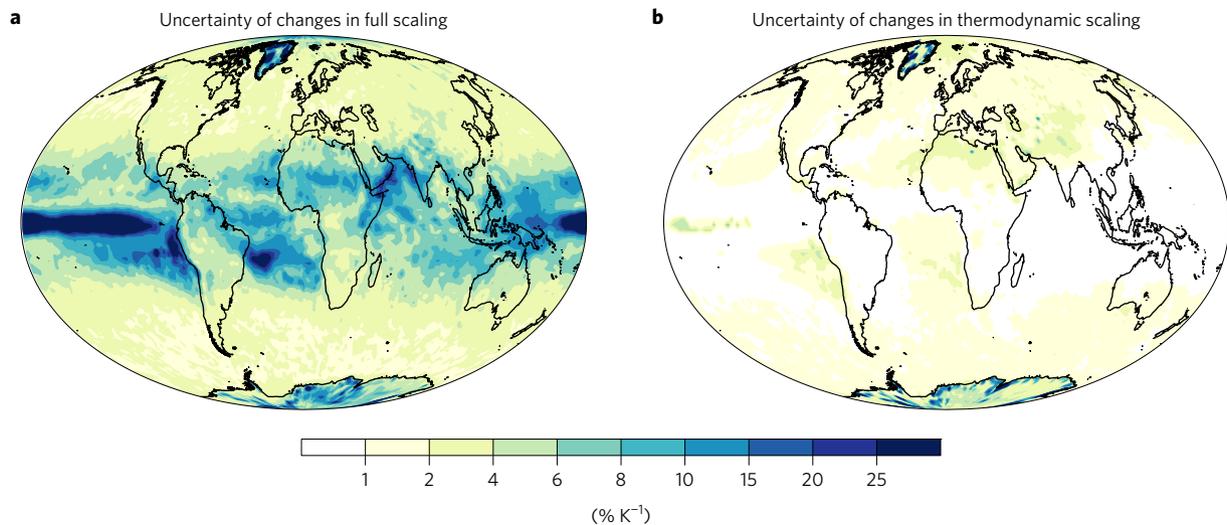
Figure 3 | Changes in thermodynamic scaling and effects of changes in vertical winds. a, Multi-model mean fractional changes in thermodynamic scaling in which the vertical velocity ω_e is kept constant (it is replaced with its mean value over the period 1950–2100). **b**, Difference between changes in full scaling and changes in thermodynamic scaling (full minus thermodynamic). Note that the maxima in the Pacific are above 60% K^{-1}. **c**, Multi-model mean fractional changes in vertically integrated saturation specific humidity q_s conditioned on the occurrence of extreme precipitation. **d**, Multi-model mean fractional changes in vertically averaged vertical velocity ω_e conditioned on the occurrence of extreme precipitation (with negative values indicating stronger ascent). Note that changes of ω_e in the lower troposphere (for example, on 700 hPa) follow a similar pattern. Stippling indicates that at least 80% of the models agree on the sign of signal. For comparison, present-day patterns of q_s and ω_e are shown in Supplementary Fig. 11.

projected to intensify with global warming in most extratropical regions and in the deep tropics, with maximum intensification rates in the tropical Pacific and the Asian monsoon region. In contrast, there are subtropical regions with little change or even decreases. Again, the scaling relationship captures this spatial pattern very well (Fig. 2b, spatial correlation of 0.96), including the regions of decreases in precipitation extremes in the subtropics. Differences between forced changes in Rx1day and in the scaling (Fig. 2c) are largest in some subtropical areas, the tropical Pacific and over the ice sheets (the scaling is not expected to yield accurate results over the ice sheets, see Methods). Correlations of spatial patterns between changes in Rx1day and the scaling in individual models are still high (>0.8, see Supplementary Fig. 3), although the differences in the correlation coefficient between the models are slightly larger than for present-day means.

Given this remarkably accurate reproduction of the spatial patterns of present-day Rx1day and its forced change, the scaling relationship can now be used to decompose this change into thermodynamic and dynamic contributions. To this end, a thermodynamic scaling is considered that also uses equation (1), but neglects time variations in the vertical velocity associated with the extreme precipitation (at each location, ω_e is replaced by its temporal average over the entire period). Forced changes in this thermodynamic scaling are consistently positive (mostly between 4 and 8% K^{-1}) and spatially relatively homogeneous, with moderate regional amplification in the Northern Hemisphere subtropics and at high latitudes (Fig. 3a). A similar spatial pattern is found for projected changes in the vertically integrated saturation specific humidity q_s conditioned on the occurrence of precipitation extremes, albeit with enhanced rates of increase (Fig. 3c). There are smaller increases in near-surface saturation specific humidity (often used to represent Clausius–Clapeyron scaling[7]) conditioned on the occurrence of precipitation extremes as found previously[8], but, compared to the thermodynamic scaling, these changes show a more pronounced land–sea contrast due to amplified surface warming over land (Supplementary Fig. 4a). This near-surface enhancement over land compared to ocean is reduced but not eliminated when actual specific humidity is used, because of a reduction in near-surface

a   Uncertainty of changes in full scaling

b   Uncertainty of changes in thermodynamic scaling

1   2   4   6   8   10   15   20   25

(% K^{-1})

Figure 4 | Uncertainty of changes in full and thermodynamic scaling. a,b, Absolute uncertainty of fractional changes in full precipitation extremes scaling (**a**) and fractional changes in thermodynamic scaling with constant vertical velocity ω_e (**b**), quantified as the standard deviation of the regression coefficients across models. Note the nonlinear scale. A similar difference between full and thermodynamic scaling is found for relative uncertainties (Supplementary Fig. 13).

land relative humidity (Supplementary Fig. 4b). The missing land–sea contrast in the thermodynamic scaling points to the fact that humidity changes at more elevated levels are most important for precipitation extremes, because of the weighting by the vertical profile of ω_e in equation (1) (refs 7,8,18). (The saturation specific humidity at 850 hPa does not exhibit such a land–sea contrast either; not shown). Increases in vertically integrated saturation specific humidity conditioned on the occurrence of precipitation extremes (Fig. 3c) are smaller than the annual-mean increases in some regions (Supplementary Fig. 5a), which can be explained by a shift of the seasonality of precipitation extremes towards the cold season (Supplementary Fig. 6a).

Although the thermodynamic response captures much of the forced response of heavy precipitation (Rx1day) in certain regions, such as the land regions in the northern mid to high latitudes, it does not explain the forced response pattern over most of the globe. Hence, variations in vertical winds are crucial for capturing the spatial pattern of Rx1day changes. Differences between changes in full and thermodynamic scaling (Fig. 3b) indicate regions where such variations in ω_e are particularly relevant, and thereby provide an estimate of the dynamic contribution. Increasing ascent velocities enhance precipitation extremes in the central Pacific and Southeast Asia. Reduced upward winds offset some of the increase of extreme precipitation intensities expected from thermodynamics in the Mediterranean region, including northern Africa and the Middle East, in Central America, Southern Africa, Australia as well as over the northern North Atlantic, and are even strong enough to robustly reverse the full response over parts of the subtropical oceans (compare Figs 2a and 3b). Broadly similar results are obtained when seasonal instead of annual precipitation maxima are considered (Supplementary Figs 7 and 8). However, the fraction of land areas with robust increases in Rx1day is smaller for seasonal compared to annual extremes, which is due to a more widespread reduction of ascent velocities, in particular over Europe and North America in boreal summer (Supplementary Fig. 8d). The estimate of the dynamic contribution to changes in annual maximum precipitation (see again Fig. 3b) is consistent with the spatial pattern obtained when considering changes in vertically averaged ω_e during precipitation extremes (Fig. 3d). These changes in conditioned vertical velocities are distinctively different in spatial pattern from changes in annual mean ω (Supplementary Fig. 5b), and this difference is

not explained by the seasonality of precipitation extremes or changes therein (Supplementary Figs 6b and 9).

To understand these regional changes in the dynamics of precipitation extremes, regionally relevant mechanisms and weather systems have to be taken into account. The dynamically induced decreases in precipitation extremes over the subtropical oceans (Figs 2a and 3b) can partly be explained by poleward shifts of the present-day pattern of ω_e in the subtropics (Supplementary Figs 10 and 11b), related to a general expansion of the Hadley cells[20]. But poleward shifts seem to explain only roughly half of the dynamical contribution, and the direct radiative response to increasing CO_2 may also contribute, as has been found previously for subtropical decreases in mean precipitation[21]. The decrease in upward velocities during precipitation extremes in the northern and southern parts of the North Atlantic storm track region, where most precipitation extremes are associated with extratropical cyclones[22], is consistent with the projected meridional contraction of the winter storm track and reduced cyclone frequencies around Iceland and in the broader Mediterranean region[23]. Also changes in cyclone intensities can play an important role—for example, in the Mediterranean[24]. In the deep tropics, the general dynamical amplification of extreme precipitation relates to an increase in upward motion and convection in a latitude band about the equator[25]. In particular, the increase in the tropical Pacific is consistent with an eastward shift of ENSO-induced rainfall[26] and a weakening of the Walker circulation[27]. The dynamical intensification of extreme precipitation in the Indian monsoon region may be related to changes in the dynamics of mesoscale monsoon depressions, but it is unclear whether these systems are well represented in CMIP5 models with their coarse spatial resolution[28]. A comprehensive representation of extreme-precipitation-producing weather systems, such as monsoon depressions, may require higher model resolution, particularly in the tropics[4]. Finally, we note that changes in dynamics and thermodynamics of precipitation extremes are not independent of each other, but physically coupled, for example, through changes in moist static stability.

Uncertainties of changes in Rx1day (Supplementary Fig. 12) and the full precipitation extremes scaling (Fig. 4a) are largest over the subtropics and tropics, consistent with previous studies that have found large uncertainties for model projections of tropical precipitation extremes[13,29]. By comparison, uncertainties of changes in the thermodynamic scaling are generally small (Fig. 4b). Thus,

the influence of thermodynamic changes on extreme precipitation, which dominates the sign of heavy precipitation changes over most land areas, is remarkably robust. However, we demonstrate that, particularly over the subtropics, tropics and oceans, the dynamic contribution strongly modifies the heavy precipitation intensification and regionally even reverses the signal. Those changes in atmospheric dynamics are also the dominant source of the uncertainty in projections of heavy precipitation (see again Fig. 4), which is consistent with uncertainty quantifications for regional projections in general[30]. Importantly, despite the large uncertainties in the amplitude of the change in precipitation extremes in the tropics (Supplementary Fig. 12), the spatial pattern of the sign of the changes in precipitation extremes is relatively robust across models (Fig. 2a).

The scaling approach applied here can provide crucial insights into regional model differences and potentially model biases, which could be disentangled into thermodynamic and dynamic bias contributions given a reliable reference data set. Such a separation into thermodynamic and dynamic contributions could inform model development, and may be useful for potential model constraints or weightings in multi-model projections of precipitation extremes. This separation could also inform alternative approaches in extreme event attribution that aim at disentangling the dynamic and thermodynamic signals[31]. By successfully providing a physically based quantification of the role of circulation for future changes in regional extreme precipitation, this study motivates further research into changes in the associated circulations, particularly in regions where the dynamic contribution is large and robust in sign. Reducing potential errors in the representation of the mechanisms underlying such dynamical changes in climate models will ultimately lead to more robust regional projections of precipitation extremes that are vital for many adaptation decisions.

Methods

Methods, including statements of data availability and any associated accession codes and references, are available in the online version of this paper.

References

1. IPCC in *Managing the Risks of Extreme Events and Disasters to Advance Climate Change Adaption* (eds Field, C. B. *et al.*) 231–290 (Cambridge Univ. Press, 2012).
2. Fischer, E. M., Beyerle, U. & Knutti, R. Robust spatially aggregated projections of climate extremes. *Nat. Clim. Change* **3,** 1033–1038 (2013).
3. Wilcox, E. M. & Donner, L. J. The frequency of extreme rain events in satellite rain-rate estimates and an atmospheric general circulation model. *J. Clim.* **20,** 53–69 (2007).
4. Rossow, W. B., Mekonnen, A., Pearl, C. & Goncalves, W. Tropical precipitation extremes. *J. Clim.* **26,** 1457–1466 (2013).
5. Trenberth, K. E. Conceptual framework for changes of extremes of the hydrological cycle with climate change. *Climatic Change* **42,** 327–339 (1999).
6. Allen, M. R. & Ingram, W. J. Constraints on future changes in climate and the hydrological cycle. *Nature* **419,** 224–232 (2002).
7. O'Gorman, P. A. Precipitation extremes under climate change. *Curr. Clim. Change Rep.* **1,** 49–59 (2015).
8. O'Gorman, P. A. & Schneider, T. The physical basis for increases in precipitation extremes in simulations of 21st-century climate change. *Proc. Natl Acad. Sci. USA* **106,** 14773–14777 (2009).
9. Sugiyama, M., Shiogama, H. & Emori, S. Precipitation extreme changes exceeding moisture content increase in MIROC and IPCC climate models. *Proc. Natl Acad. Sci. USA* **107,** 571–575 (2010).
10. Emori, S. & Brown, S. J. Dynamic and thermodynamic changes in mean and extreme precipitation under changed climate. *Geophys. Res. Lett.* **32,** L17706 (2005).
11. Chen, G., Ming, Y., Singer, N. D. & Lu, J. Testing the Clausius–Clapeyron constraint on the aerosol-induced changes in mean and extreme precipitation. *Geophys. Res. Lett.* **38,** L04807 (2011).
12. Kharin, V. V., Zwiers, F. W., Zhang, X. & Wehner, M. Changes in temperature and precipitation extremes in the CMIP5 ensemble. *Climatic Change* **119,** 345–357 (2013).
13. Pendergrass, A. G. & Hartmann, D. L. Changes in the distribution of rain frequency and intensity in response to global warming. *J. Clim.* **27,** 8372–8383 (2014).
14. Westra, S., Alexander, L. V. & Zwiers, F. W. Global increasing trends in annual maximum daily precipitation. *J. Clim.* **26,** 3904–3918 (2013).
15. Fischer, E. M. & Knutti, R. Detection of spatially aggregated changes in temperature and precipitation extremes. *Geophys. Res. Lett.* **41,** 547–554 (2014).
16. Donat, M. G., Lowry, A. L., Alexander, L. V., O'Gorman, P. A. & Maher, N. More extreme precipitation in the world's dry and wet regions. *Nat. Clim. Change* **6,** 508–513 (2016).
17. Fischer, E. M., Sedláček, J., Hawkins, E. & Knutti, R. Models agree on forced response pattern of precipitation and temperature extremes. *Geophys. Res. Lett.* **41,** 8554–8562 (2014).
18. Muller, C. J., O'Gorman, P. A. & Back, L. E. Intensification of precipitation extremes with warming in a cloud-resolving model. *J. Clim.* **24,** 2784–2800 (2011).
19. Singh, M. S. & O'Gorman, P. A. Influence of microphysics on the scaling of precipitation extremes with temperature. *Geophys. Res. Lett.* **41,** 6037–6044 (2014).
20. Vallis, G. K., Zurita-Gotor, P., Cairns, C. & Kidston, J. Response of the large-scale structure of the atmosphere to global warming. *Q. J. R. Meteorol. Soc.* **141,** 1479–1501 (2015).
21. He, J. & Soden, B. J. A re-examination of the projected subtropical precipitation decline. *Nat. Clim. Change* **7,** 53–57 (2017).
22. Pfahl, S. & Wernli, H. Quantifying the relevance of cyclones for precipitation extremes. *J. Clim.* **25,** 6770–6780 (2012).
23. Zappa, G., Shaffrey, L. C., Hodges, K. I., Sansom, P. G. & Stephenson, D. B. A multimodel assessment of future projections of North Atlantic and European extratropical cyclones in the CMIP5 climate models. *J. Clim.* **26,** 5846–5862 (2013).
24. Zappa, G., Hawcroft, M. K., Shaffrey, L., Black, E. & Brayshaw, D. J. Extratropical cyclones and the projected decline of winter Mediterranean precipitation in the CMIP5 models. *Clim. Dynam.* **45,** 1727–1738 (2015).
25. Lau, W. K. M. & Kim, K.-M. Robust Hadley Circulation changes and increasing global dryness due to CO_2 warming from CMIP5 model projections. *Proc. Natl Acad. Sci. USA* **112,** 3630–3653 (2015).
26. Huang, P. Time-varying response of ENSO-induced tropical Pacific rainfall to global warming in CMIP5 models. Part I: multimodel ensemble results. *J. Clim.* **29,** 5763–5778 (2016).
27. Vecchi, G. A. *et al.* Weakening of tropical Pacific atmospheric circulation due to anthropogenic forcing. *Nature* **441,** 73–76 (2006).
28. Turner, A. G. & Annamalai, H. Climate change and the South Asian summer monsoon. *Nat. Clim. Change* **2,** 587–595 (2012).
29. O'Gorman, P. A. Sensitivity of tropical precipitation extremes to climate change. *Nat. Geosci.* **5,** 697–700 (2012).
30. Shepherd, T. Atmospheric circulation as a source of uncertainty in climate change projections. *Nat. Geosci.* **7,** 703–708 (2014).
31. Trenberth, K. E., Fasullo, J. T. & Shepherd, T. G. Attribution of climate extremes. *Nat. Clim. Change* **5,** 725–730 (2015).

Acknowledgements

Author contributions

S.P. initiated the study, performed the analysis based on code provided by P.A.O'G. and drafted the paper. All authors discussed the results and edited the manuscript.

Additional information

Competing financial interests

The authors declare no competing financial interests.

Methods

CMIP5 model data and analysis. Climate-model output from the Coupled Model Intercomparison Project Phase 5 (CMIP5) archive is analysed, using all models that provide the required data for the historical period 1950–2005 and the RCP8.5 scenario simulation covering 2006–2100. Daily accumulated surface precipitation, daily mean temperature and vertical wind velocity on all available vertical pressure levels, daily mean temperature and specific humidity at 2 m above ground as well as monthly mean surface pressure are extracted from the CMIP5 database. These data are available from 22 models, 4 of which provide data from several initial condition ensemble members (see Supplementary Table 1). Note that the 2-metre temperature and humidity fields are not available from the CMCC-CESM, CMCC-CM, CMCC-CMS, FGOALS-g2, MPI-ESM-LR and MPI-ESM-MR models. The analysis is performed on each model's native grid, and the resulting fields are interpolated on a $1° \times 1°$ geographical grid for the calculation of multi-model ensemble means and uncertainties. Different initial condition members of the same model are treated separately and are given a reduced weight when calculating multi-model averages and standard deviations (such that each model contributes equally to the multi-model mean, independent of the number of its ensemble members). At each model grid point, the annual maximum daily precipitation Rx1day is determined for each year of the analysis period 1950–2100. Vertical profiles of daily average temperature and vertical wind on pressure levels at the location and on the day of this maximum precipitation are used as input for the scaling analysis. On each level, q_s is calculated from a modified Tetens formula[32] with interpolation of the saturation vapour pressure between the ice and liquid phase in a temperature range between $-23\,°C$ and $0\,°C$. The vertical integral is performed over all tropospheric levels with ascent ($\omega_e < 0$). The troposphere is defined as all pressure levels below the highest level with a lapse rate of $2\,K\,km^{-1}$ and below 50 hPa. This definition of the tropopause does not yield reasonable results over Greenland and Antarctica, where the atmosphere is generally very stable, and the results are thus less reliable. In these regions, all levels below 50 hPa are used. Note that, in contrast to ref. 8, we use the vertical velocity on pressure levels from the model output rather than having to compute it from the continuity equation, since ω_e output is directly available from the models.

Following ref. 17, the forced response of annual maximum precipitation and the corresponding scaling to global warming is estimated by calculating linear regressions of the relative change at each grid point (with respect to the mean in the historical period 1950–2005) against global mean near-surface temperature of the respective model, using annual data for the entire analysis period 1950–2100. In general, this yields more robust results than evaluating differences in multi-decadal means[17]. When analysing seasonal instead of annual precipitation maxima (Supplementary Figs 7 and 8), some models simulate very low precipitation amounts at certain grid points in the subtropics, which leads to spurious relative changes. Such grid points (where the seasonal maximum precipitation averaged over the historical reference period is smaller than 0.2 mm) are not taken into account in the multi-model mean.

The agreement of spatial patterns of precipitation extremes and the precipitation extremes scaling, as well as of changes therein, is measured using area-weighted spatial correlation coefficients and root mean square differences. To obtain weighted correlation coefficients, the weighted covariance $\mathrm{cov}(\mathbf{x}, \mathbf{y}; \mathbf{w})$ of two vectors $\mathbf{x}$ and $\mathbf{y}$ with spatial weights $\mathbf{w}$ is calculated as

$$\mathrm{cov}\left(\mathbf{x}, \mathbf{y}; \mathbf{w}\right) = \frac{\sum_i w_i \left(x_i - \bar{x}\right)\left(y_i - \bar{y}\right)}{\sum_i w_i} \quad (2)$$

where $\bar{x}$ and $\bar{y}$ denote the weighted means of $\mathbf{x}$ and $\mathbf{y}$, respectively. Note that regression coefficients can become very large at specific grid points where the historical mean is close to 0. Such grid points are removed before calculating spatial correlations using a threshold of $\pm\,100\%\,K^{-1}$; the fraction of points that is omitted is always smaller than 1%. The uncertainty of a signal in the multi-model ensemble is quantified as the local standard deviation across models, and the relative uncertainty as the ratio of this standard deviation to the absolute value of the multi-model mean change.

Comparison with observation-based data. To evaluate the representation of annual maximum precipitation in the CMIP5 climate models, we use data from the Global Precipitation Climatology Project (GPCP) One-Degree Daily (1DD) dataset[33] for the period 1997–2014. This dataset contains precipitation estimates from a combination of multiple satellite observations, which over land are adjusted

based on monthly rain gauge measurements. To obtain a spatial resolution that is comparable to the CMIP5 models, the data are regridded from the original one-degree resolution to a $2° \times 2°$ grid by averaging over adjacent grid points. The annual maximum precipitation from this dataset is shown in Supplementary Fig. 14. Over land, spatial pattern and absolute values of this observation-based estimate of Rx1day agree reasonably well with the CMIP5 multi-model mean (Fig. 1a), with some regional differences, for example, over Anatolia and the Indian monsoon region. Over the oceans, CMIP5 values are generally biased high compared to GPCP, and there are larger differences in spatial patterns over the tropical Indian Ocean and the tropical Pacific (where several CMIP5 models have a 'double ITCZ' bias[34]). Furthermore, there is an apparent discontinuity in the observational estimate at $40°$ latitude, where the GPCP primary data source and algorithm change. In general, this model-data comparison should be interpreted with care due to the substantial uncertainties associated with estimates of extreme precipitation from gridded observational data[35]. Over the ocean, where GPCP data are not constrained by surface measurements, these uncertainties are even larger than over land.

To test the scaling relationship based on data with larger observational constraints than the CMIP5 simulations, we use ERA-Interim reanalyses[36] for the period 1979–2015. Daily mean temperature and vertical pressure velocity on model levels as well as surface pressure and precipitation from the reanalysis are regridded to the same $2° \times 2°$ grid as used for the GPCP analysis by averaging over adjacent grid points (with an original grid spacing of $1°$). Note that ERA-Interim precipitation is a forecast product and, to exclude potential effects of model spin-up, forecast steps larger than 6 h are used here. Daily precipitation amounts are obtained by combining data from different forecasts (the accumulated precipitation between forecast hours 12 and 18 from the forecast started at 12 UTC on the previous day, between hours 6 and 18 from the 00 UTC forecast and between hours 6 and 12 from the 12 UTC forecast). Annual maximum precipitation is determined at each grid point and in each year, and the scaling analysis (equation (1)) is applied in the same way as for the CMIP5 data. As shown in Supplementary Fig. 15a, Rx1day from ERA-Interim is similar to the CMIP5 multi-model mean (Fig. 1a) in many regions, but does not suffer from a 'double ITCZ' bias over the Pacific and is closer to the GPCP satellite estimates over the Indian Ocean, western Pacific and Maritime Continent (where CMIP5 models simulate excessively large Rx1day values). The precipitation extreme scaling (Supplementary Fig. 15b) very accurately reproduces the spatial pattern of ERA-Interim Rx1day, but overestimates precipitation amounts in dry regions and underestimates them in moist regions. This is very similar to the CMIP5 results, and further supports the suitability of the scaling approach for studying spatial patterns of extreme precipitation.

A scaling analysis based on ERA-Interim data is not able to reproduce the GPCP annual precipitation maxima, but this is not because of problems with the scaling methodology: the scaling is able to reproduce the average of precipitation amounts from the ERA-interim reforecasts on the days of GPCP annual maxima, but the ERA-Interim reforecasts underestimate the GPCP precipitation amounts on those days (not shown).

References

32. Simmons, A. J., Untch, A., Jakob, C., Kallberg, P. & Undén, P. Stratospheric water vapour and tropical tropopause temperatures in ECMWF analyses and multi-year simulations. *Q. J. R. Meteorol. Soc.* **125,** 353–386 (1999).
33. Huffman, G. J. *et al*. Global precipitation at one-degree daily resolution from multi-satellite observations. *J. Hydrometeorol.* **2,** 36–50 (2001).
34. Xiang, B., Zhao, M., Held, I. M. & Golaz, J.-C. Predicting the severity of spurious "double ITCZ" problem in CMIP5 coupled models from AMIP simulations. *Geophys. Res. Lett.* **44,** 1520–1527 (2017).
35. Herold, N., Behrangi, A. & Alexander, L. S. Large uncertainties in observed daily precipitation extremes over land. *J. Geophys. Res.* **122,** 668–681 (2017).
36. Dee, D. P. *et al*. The ERA-Interim reanalysis: configuration and performance of the data assimilation system. *Q. J. R. Meteorol. Soc.* **137,** 553–597 (2011).